3D printed instrumentation for point-of-use leaky waveguide (LW) biochemical sensor

Goddard, Nicholas J.; Dixon, Hazel; Toole, Nicola; Gupta, Ruchi

DOI:
10.1109/TIM.2020.2969036

3D Printed Instrumentation for Point-of-Use Leaky Waveguide (LW) Biochemical Sensor

Nicholas J. Goddard, Process Instruments (UK) Ltd, March Street, Burnley, BB12 0BT, UK; Email: nick.goddard@processinstruments.net.
Hazel J. Dixon, School of Chemistry, University of Birmingham, Birmingham, B15 2TT, UK; Email: hjd839@student.bham.ac.uk.
Nicola Toole, School of Chemistry, University of Birmingham, Birmingham, B15 2TT, UK; Email: nxt900@student.bham.ac.uk.
Corresponding author: Ruchi Gupta, School of Chemistry, University of Birmingham, Birmingham, B15 2TT, UK; Email: r.gupta.3@bham.ac.uk.

Keywords: Leaky waveguide, 3D printing, refractive index, sensor, point-of-use

Abstract

Leaky waveguide (LW) biosensors enable accurate measurements using small sample volumes and are cheap to produce, hence are advantageous in the area of point-of-use devices. Yet, current instrumentation to test LW chips is both bulky and costly, because of the use of expensive components such as glass optics and manufacturing techniques such as computer numerical control (CNC) machining. Meanwhile, 3D printing allows the production of complex shapes that cannot be realised using these techniques, while injection moulding allows the low cost production of optical components. 3D printed instruments offer huge advantages over traditional laboratory instrumentation, in terms of the cost of the manufacturing equipment required, the cost of the resulting instrumentation, size, and portability. This study describes the design and manufacture of a novel 3D printed biosensor instrument, and demonstrates its use for bioanalysis using LWs with a chitosan waveguide layer. This instrument has a refractive index resolution comparable to laboratory instrumentation and 3D printed surface plasmon resonance (SPR) instruments (2.37×10^{-6}, 5.90×10^{-6} and 1.7×10^{-6} refractive index units [RIU] respectively) and has proven able to detect 133 nM (nmol L^{-1}) levels of Immunoglobulin G (IgG) *via* the measurement of the change in resonance angle produced upon the protein binding to the film.

I. Introduction

Point-of-use biochemical analytical systems have a potential to revolutionise human health, environmental monitoring and food security [1-4]. The widespread adoption of biochemical analytical systems at point-of-use requires that both sensors and associated instrumentation are low cost and portable, while offering a performance comparable to equivalent laboratory based

measurement platforms. Optical leaky waveguide (LW) sensors are potentially low cost as they can be fabricated on float glass or injection moulded substrates by spin coating of natural or synthetic hydrogels [5-8]. This avoids the cost of vacuum processing needed for deposition of gold for surface plasmon resonance (SPR) [9] or high index dielectric materials for conventional waveguide sensors [10-14]. As shown in Figure 1 (a), light is partially confined in a planar LW using total internal reflection (TIR) and Fresnel reflection at sample/waveguide and substrate/waveguide interfaces in LWs. The mode equation for LW is given by [6]:

$$(2m-1)\lambda = \frac{4\pi h}{\lambda}\left(\sqrt{n_w^2 - N^2}\right) - 2\tan^{-1}\left(\frac{n_w^{2p}}{n_c^{2p}}\sqrt{\frac{N^2-n_c^2}{n_w^2-N^2}}\right) \quad (1)$$

where h is waveguide thickness (m), λ is wavelength (m), n_w, n_c and N are waveguide, sample and effective refractive index (RI) respectively, p is 0 for transverse electric (TE) and 1 for transverse magnetic (TM) modes, and m is an integer. The number of solutions for N corresponds to the number of optical modes supported by a waveguide. Additionally, the resonance angle (θ_R) of the waveguide is given by [15]:

$$\theta_R = \sin^{-1}\left(\frac{N}{n_s}\right) \quad (2)$$

where n_s is the substrate RI. θ_R of LWs may be visualised either by depositing a metal layer between substrate and waveguide [7, 16, 17] or fabricating a discontinuous waveguide [18] or incorporating a dye such as reactive blue 4, which absorbs over a significant part of the visible spectrum, in the waveguide [6, 8, 19]. In this work, a dye doped waveguide was used because this approach offers simplicity of fabrication and affordability. In this case, a dip in the reflectivity curve (Figure 1 (b)) was observed at θ_R. For fixed h and λ, N and hence θ_R are a function of n_c and n_w that may change as a result of introducing sample solutions of different RI on/ in the waveguide and/ or binding of analyte to bioreceptors immobilized in the waveguide. Shifts in θ_R are, therefore, monitored to determine the concentration of analytes (Figure 1 (c)). This shift is proportional to the refractive index change and hence to the change in concentration of the analyte.

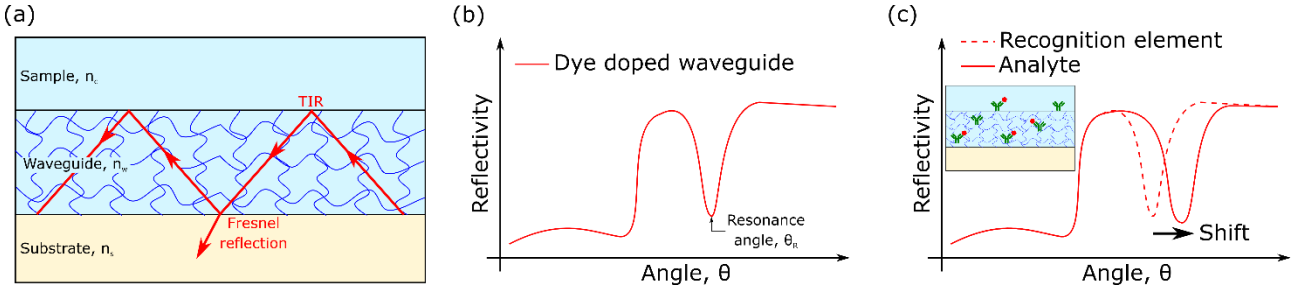

Figure 1: (a) Image depicting confinement of light *via* TIR and Fresnel reflection in a theoretical LW where $n_s > n_w > n_c$ (b) schematic of reflectivity curve of dye-doped LW as a function of angle of incidence (θ) and (c) concept of biochemical sensing using the LW

LWs offer the following major benefits for biochemical sensing:

(1) Closely-coupled internal referencing for significant rejection of common-mode effects (i.e. variations in temperature, bulk refractive index, emission wavelength of the light source and mechanical perturbations) while measuring analyte-recognition element interactions. We have shown that stacked sensor and reference LWs where vertical centre-to-centre distance was 1-2 μm between the waveguides, allowed rejecting the effect of temperature and bulk refractive index by factors of 20 and 50 respectively [7].

(2) Ease of integration with electric field driven sample processing because LW is an all-dielectric structure. This is in contrast to SPR where the presence of continuous gold film will short any electric field applied parallel to the sensor surface. Electric field driven sample processing allows analyte pre-concentration to improve the limit of detection and reduce the response time. We have shown that the approach can provide pre-concentration factors between 600 and 930 in 60 s [20].

(3) Broad wavelength range (320 to 900 nm) of operation unlike SPR, which typically works at wavelength above 600 nm. We have shown that this broad wavelength range of operation of LWs allowed determining average iron content of ferritin, which is an important biomarker of injury, inflammation or infection [21] in a single step. Determining the average iron content of ferritin in a *single step* is not possible with current state of art method (i.e. enzyme-linked immunosorbent assay, ELISA) used in clinics [8].

The instrumentation associated with LW sensors has so far been bulky (~60×60×35 cm), heavy (~25 kg) and fabricated by subtractive methods such as milling from typically aluminium and steel for strength and rigidity [8, 20, 22]. Subtractive methods are often used to create multiple parts that are then assembled into a final instrument because of the limitations of the fabrication method. This in turn adds to the cost of the resulting instrument. In contrast, additive manufacturing/ 3D printing offers the ability to produce almost arbitrarily complex shapes with undercuts and hollow interiors that are impossible to produce in a single part by other methods [23]. These methods include stereolithography apparatus (SLA), fused filament fabrication (FFF), ink-jet printing, and selective laser sintering (SLS), which reduce waste and provide ease of design along with speed of development. When allied with techniques such as injection moulding for producing optical and some mechanical components, a large proportion of an optical instrument may be constructed rapidly without recourse to waste-generating methods. In many cases, 3D printed parts are made

with different infill density to reduce print time and material usage without significantly affecting the structural strength of the part. The range of materials that can be printed is constantly expanding, and includes polymers, ceramics, and metals [24-26]. As a result, 3D printing has increasingly been used to develop a wide range of biochemical analytical systems [27-29]. For example, 3D printing has been used to develop point-of-use instrumentation for SPR with a resolution of 6.4×10^{-6} to 10^{-4} RIU^{-1} [30, 31]. The low cost of SLA and FFF 3D printers means that instruments can be produced in low resource settings without requiring dedicated production lines, and that designs can be modified quickly as requirements change.

Further development of additive manufacturing will enable an even larger proportion of an instrument to be 3D printed. For example, Nano Dimension (Ness Ziona, Israel) have produced an ink-jet printer that can produce multilayer printed circuit boards along with some passive components such as capacitors and inductors. It is likely that a wider range of components will be 3D printed in the near future, although it is unlikely that active components will be 3D printed for some time yet. Similarly, optical components such as lenses require smooth surfaces that are currently difficult to produce without post-processing. These components can, however, be mass produced at low cost by injection moulding.

The focus of this work has been to demonstrate a 3D printed read-out instrument for LW biochemical sensors that is affordable, portable and easy to use. The instrument was produced using a low-cost FFF printer using commercially available filament and as far as possible off-the shelf and standard components. The only custom component not produced by 3D printing was the printed circuit board for the electronics. This work showed that the resolution in refractive index units (RIU) of the 3D printed instrument was comparable to the existing laboratory based instrumentation fabricated by CNC machining (2.37×10^{-6} *versus* 5.90×10^{-6} RIU respectively). The RI resolution of the LW obtained using the 3D printed instrument reported in this work was comparable to the values reported in literature for 3D printed SPR instruments shown in Table 1 (2.37×10^{-6} RIU *versus* 1.7×10^{-6} to 10^{-4} RIU). The response of the LW to glycerol solutions of different refractive index varied by <10% for area-to-area and device-to-device. Finally, we demonstrated the suitability of LW and its associated 3D printed instrument for protein sensing using streptavidin, biotin anti-Immunoglobulin G (anti-IgG) and Immunoglobulin G (IgG) as exemplar analytes.

Sensing mechanism, year	**RI resolution/ limit of detection**	**Size, weight**	**Limitations**
SPR *via* phone camera, 2014	$5x10^{-5}$ RIU	Not Available	Complex sensor design 3D printed part is just a rest

[32]			for a smartphone
SPR with lab-on-chip, 2016 [33]	$6x10^{-5}$ RIU	150 mm × 60 mm × 170 mm, <500 g	Uses a complex nanohole SPR array
Electrochemical (Screen printed electrochemical sensors, SPES), 2017 [34]	2 ng/mL	sensor 51 mm × 51 mm, printed circuit board 76 mm × 33 mm, bluetooth module 75 mm × 70 mm × 45 mm	Not label-free Requires two antibodies
Interferometry *via* phone camera, 2018 [35]	Not Available	140 mm × 165 mm × 50 mm	Has not been tested with proteins Requires a specific smartphone
SPR with wavelength readout, 2018 [30]	10^{-4} RIU	50 mm × 70 mm × 55 mm	Poor resolution
Mechanically-scanned SPR, 2018 [31]	6.4×10^{-6} RIU	Not Available	Slow mechanical scanning Backlash
Resonant Mirror, 2019 [36]	$1.7x10^{-6}$ RIU 583 nm/RIU	Not Available	Requires vacuum deposition of waveguide
This work	2.37×10^{-6} RIU	162×130×107 mm (all with a precision of 0.5 mm) and 825.05±0.005 g	Requires high porosity hydrogel waveguide

Table 1: Comparison of some 3D printed biosensor instruments reported in literature and this work

II. Experimental

Chemicals and materials: Ethanol, 1M acetic acid, methanol, 25% (v:v) glutaraldehyde (GA), reactive blue 4 (RB4), (4-(2-hydroxyethyl)-1-piperazineethanesulfonic acid) (HEPES), 1 M sodium hydroxide (NaOH), bovine serum albumin (BSA, A2153), biotin anti-Immunoglobulin G (anti-IgG) (B3773) and Immunoglobulin G (IgG) (I5131) were bought from Sigma-Aldrich (Gillingham, UK). Decon 90, Glycerol (M_w: 92) and chitosan (M_w: 100,000-300,000, 90% deacetylated) were purchased from Fisher (Loughborough, UK). Syringe filters with 5 µm size cut-off were bought

from Scientific Lab Supplies (Nottingham, UK). Streptavidin (2-0203-100-IBA) was purchased from Stratech Scientific (Ely, UK).

The carbon fibre-filled polylactic acid (CF-PLA) and black polylactic acid (PLA) filaments were bought from Proto Pasta (Vancouver, WA, USA) and 3DfilaPrint (Essex, UK) respectively. A NEMA8 bipolar stepper motor (SCA2018S0604-A) was purchased from Nanotec (Feldkirchen, Germany), and a 100:1 reduction worm gear (worm ZW0.4-1, wheel ZM0.4-100) was bought from HPC Gears (Chesterfield, UK). A bipolar captive linear stepper motor (LC1574W-V) was bought from Haydon Kerk Pittman (Connecticut, USA).

LW fabrication and flow cell: Glass slides were cut into squares where the dimension of each side was 25.4±0.5 mm and cleaned in Decon 90, water and ethanol for 30 min each in an ultrasonic bath. Chitosan was first purified by adapting a method from [37]. The chitosan was dissolved as a 1% (w:v) solution in 0.1 M acetic acid with magnetic stirring for 18 h following which the solution was filtered through the 5 µm syringe filters. Excess 1 M NaOH(aq) was added to form an off-white precipitate. The precipitate was collected after four rounds of centrifuging, and then dialysed for 5 days against deionised water. The precipitate was washed further with deionised water and methanol, and separated by centrifuging. Excess methanol was removed by rotary evaporation, and water was removed by freeze drying for 24 h. The dry purified chitosan was collected as off-white flakes in a ~60% yield.

The purified chitosan was re-dissolved in 0.1 M acetic acid with magnetic stirring for 18 h to form a 1% (w:v) solution. 100 µL of this solution was spin coated on to clean glass slides at a spin speed of 900 rpm with an acceleration of 100 rpm/s for 30 s. The slide was placed in an incubator at humidity of 75-80% and temperature of 25 °C for 3 minutes. 0.03125% (v:v) GA solution was prepared by diluting 25 µl of 25% (v:v) GA stock solution to 20 ml using 100 mM HEPES buffer, pH 7.4. Subsequently, the slides were immersed in a 0.03125% (v:v) GA solution in 100 mM HEPES buffer, pH 7.4 for 10 minutes to crosslink the chitosan film. The slides were washed in 100 mM HEPES buffer, pH 7.4. To visualise the resonance angle of the LWs, the chitosan films were stained with 0.1 mM RB4 solution in 100 mM HEPES buffer, pH 7.4 for 5 minutes. Chitosan films were stored wet in 100 mM HEPES buffer, pH 7.4 in petri dishes covered with aluminium foil until being used.

A flow cell was made by CNC machining a 3 mm thick black PMMA forming a recessed circular cavity of diameter of 18 mm and 0.2 mm deep surrounded by a groove 1 mm wide and 0.75 mm deep in which an O-ring was mounted. The plate was placed on the waveguide and held in place using a 3D printed fixture.

Methodology: A 3D CAD model of the instrument was created using AutoCAD (Autodesk Inc, San Rafael, CA, USA) and individual components were exported as STL files for slicing using Simplify3D slicing software (Cincinnati, OH, USA). All of the printed components were made using a Flashforge Creator Pro printer (Flashforge Corp, Jinhua, China).

Fluids were pumped through the flow cell using a peristaltic pump (Minipuls® 3, Gilson, Bedfordshire, UK) at a flow rate of 0.2 ml min^{-1}. The RI of the solutions were measured using RFM900-T refractometer (Bellingham and Stanley, Kent, UK) with an accuracy of $\pm 1\times10^{-5}$. The laboratory based instrumentation was fabricated using CNC machining and has been previously described [5-8, 16-19].

Chitosan films deposited on glass substrates were placed on a BK7 equilateral prism using RI matching oil. The role of the RI matching oil was to avoid an air gap between prism top and substrate bottom, which would otherwise lead to stray reflections. The flow cell was mounted on top of the LW sensor. The glycerol solutions of different concentrations and hence RI were introduced on the top of the LW, and $\Delta\theta_R$ was monitored in real-time using both the laboratory based and 3D printed instruments.

Protein immobilisation was carried out as follows: 0.2% GA (30 min), 10 mg mL^{-1} streptavidin (2.5 h), 5 mg mL^{-1} BSA (30 min), 0.012 mg mL^{-1} biotin anti-IgG (1 h), and 0.02 mg mL^{-1} IgG (2 h) were added consecutively, and 100 mM, pH 7.4 HEPES buffer was used to wash the channel between each step until stable. The chitosan waveguide and streptavidin contained primary amines, which can react with the aldehydes on either ends of GA. Thus, we used GA as a linker to attach streptavidin within the chitosan LW. Immunoglobulin G (IgG) is a protein that is secreted by B-lymphocytes to recognise foreign proteins and thus fight infection [38]. An antibody against IgG (i.e. anti-IgG) tagged with biotin, which binds strongly to streptavidin, was introduced next to attach anti-IgG to the LW. Anti-IgG has complementarity determining regions (CDRs), which recognize and bind IgG. Thus, IgG was introduced to allow it to bind to immobilized anti-IgG. The reaction and binding between different species was monitored in real-time by recording the shifts in the resonance angle of the LW.

III. Results and Discussion

3D printed Instrumentation and software*:* The challenge when miniaturizing an optical biosensor instrument is to maintain the same or better performance than the larger (and considerably more expensive) bench instruments. 3D printing using carbon fibre-filled polylactic acid (CF-PLA) provides the high rigidity structures needed to prevent unwanted movement of the optical components. In addition, 3D printing permits very complex shapes to be produced that cannot easily be fabricated in one piece by subtractive methods. In the instrument described here, only four

printed components were needed for the complete optical system. Minimizing the number of component parts means that the opportunities for misalignment of parts are reduced. To reduce the size of the instrument and thus permit it to be fabricated using the available 3D printer, the optical path to the camera was folded using a rotating mirror, which also allowed the range of angles falling on the camera to be selected. This, in turn, allowed the full angular dynamic range of the camera to be utilized by ensuring that the resonance dip at the start of a run was close to low angle end of the image sensor and moved to higher angles as material bound to the waveguide.

A photo of the 3D printed instrument is provided in Figure 2. The dimensions and weight of the instrument was 162×130×107 mm (all with a precision of 0.5 mm) and 825.05±0.005 g respectively. The structure that was used to hold the various motors, mechanical, optical and electronic components was made of CF-PLA filament to provide high rigidity. The fill factor was 25% to reduce material usage and reduce the part build time but still provide high rigidity. As shown in Figure 2, the mirror was rotated using a NEMA8 bipolar stepper motor driving a 100:1 reduction worm gear to provide a full step rotation at the mirror of 0.018°. Similarly, the camera was mounted on a CF-PLA 3D printed holder, which could be moved from side to side using a bipolar captive linear stepper motor with 20 µm full step size. Optical interrupters were used to determine the home positions for the mirror and camera. The case and base of the instrument were printed from black PLA filament as these did not require the high rigidity of CF-PLA.

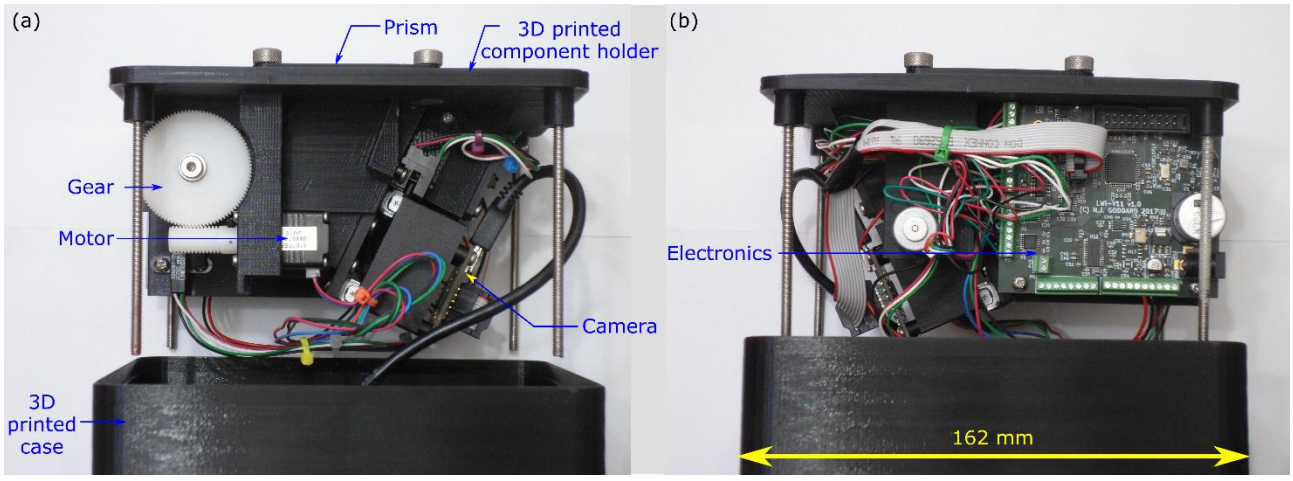

Figure 2: Exploded image of the 3D printed instrument showing (a) mechanical components and (b) electronics

As shown in Figure 3, the light source was a 650 nm point source LED (MTPS8065WC, Marktech Optoelectronics Inc, Latham, NY, USA) with an 80 µm circular emission area and a typical optical output power of 1 mW at 20 mA drive current. The output of this LED was collimated using a plastic aspheric lens (Knight Optical, Maidstone, UK), TE polarised using a

plastic polariser (32WL100, Comar Optics, Cambridge, UK) and finally focused into a wedge beam using a 25 mm focal length cylindrical lens (25 YQ 25, Comar Optics, Cambridge, UK) giving a range of angles of incidence of 58.6 to 71.4°. The wedge beam was coupled into the waveguide *via* a BK7 equilateral prism with 38.1 mm square faces (Optotronics Inc, Mead, CO, USA). The out-coupled light was directed onto a 10 Mpixel USB2 camera (UI-1492-LE, IDS Imaging, Obersulm, Germany) by a rotatable λ/4 front surface mirror (40 MX 25, Comar Optics Ltd, Cambridge, UK). The size of each camera pixel was 1.67 µm × 1.67 µm. The camera had an active area of 6.44 by 4.616 mm and was at a distance of 151.46 mm from the sensor, thus subtending an angle of 2.436°. To permit the camera to capture waveguide resonances over a wide angle range, the mirror could be rotated by ±7.5° around a centre angle of 65°, giving an output angle range of 50 - 80°. The mirror mount was preloaded by a spring to avoid backlash in the worm gear. The camera mount could be translated sideways by ±4 mm with a step size of 20 µm to cope with slight misalignments of the mirror and sensor chip.

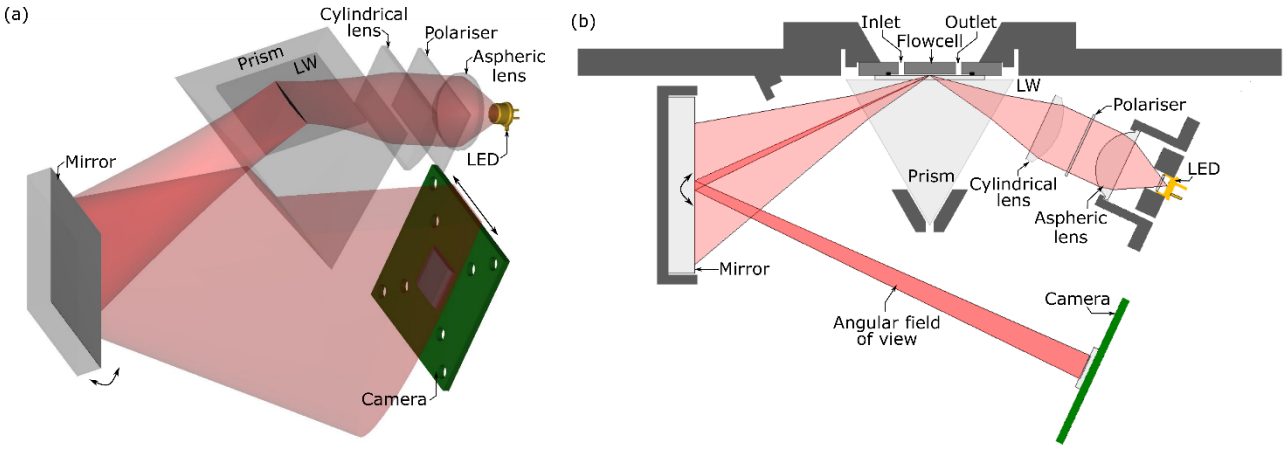

Figure 3: A schematic showing the light source, optical components and detector including the light path (a) 3D (flowcell was not shown for clarity) and (b) side views (where the mirror could be rotated and camera could be moved from side to side)

To control the stepper motors and light source, a four layer control PCB was designed and fabricated. This used an XMOS XLF208-256-TQ64-C10 8-core processor with 256K of RAM and 1M of flash memory running at 500 MHz (XMOS, Bristol, UK). Each core uses hardware scheduling to guarantee a minimum of 62.5 MIPS. Software for the processor was developed using the xTIMEComposer integrated development environment and written in the XC language, which is a variant of the C programming language with additional constructs for parallel programming, inter-

core communications and input/output operations. Communication with the host PC was *via* the camera board's I^2C interface. The board block diagram is given in Figure 4.

PC software to control the instrument was written using C++Builder (version 10.1, Embarcadero Technologies, Austin, TX, USA). Briefly, the software allows timed capturing of images from the camera, after which the averaged intensity profiles in user-selected areas are generated and used to determine the position of the resonance angle in that portion of the image. These positions are displayed in a chart recorder-like format covering the previous 1000 image captures and also saved on disk in comma separated values (CSV) format for subsequent processing. In addition, a separate window provides controls for the angular position of the mirror, the position of the camera, the source LED current, and the temperature of the sensor.

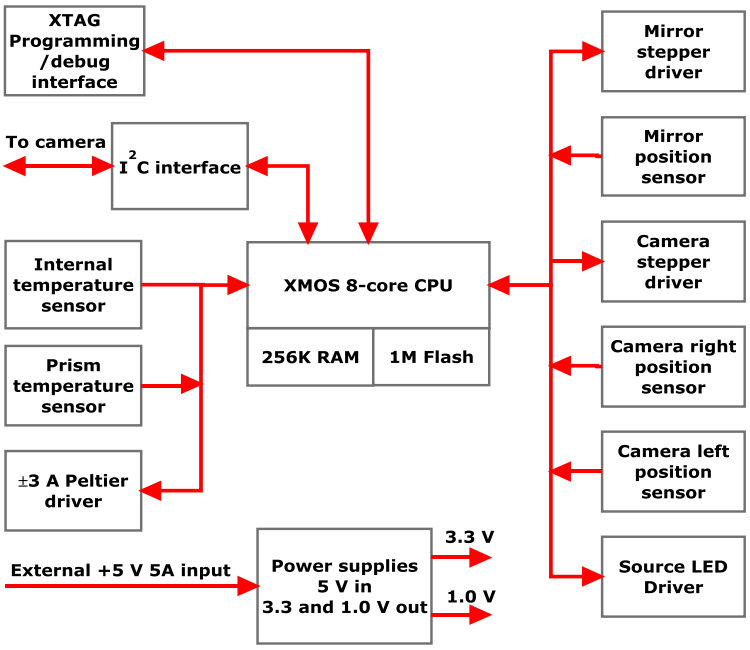

Figure 4: Block diagram of electronics in the 3D printed LW instrumentation

LW Optimization and characterization: As discussed in our previous work [8], 1% (w:v) chitosan solution spun at 900 rpm was optimum to obtain uniform thin films capable of supporting an optical mode. Similarly, the drying time between spin coating and subsequent rehydration was set to 3 min to obtain films that are porous to macromolecules such as proteins [8]. A typical output of the LW captured using the 3D printed instrument is provided in Figure 5 (a) where the x- and y-axis represent the angle of incidence and distance along the width of the microchannel respectively. The position at which the black line is observed corresponds to the resonance angle. A dip in the reflectivity curve of the LW is observed at the resonance angle because of the presence of an absorbing dye (in this case, RB4) in the chitosan waveguide. The variations in the resonance angle

along the width of the channel are a result of the non-uniformities in the thickness of the chitosan film. A plot of average gray scale value, which is indicative of the reflectivity of the LW, *versus* angle of incidence is provided in Figure 5 (b). The thickness and refractive index of chitosan film was estimated to be 1.54 µm and 1.3451 based on previous work [8], and the concentration of RB4 immobilized in the waveguide was 3.6 mM. This implies that 6.4% of the primary amines in the chitosan film were occupied by the dye.

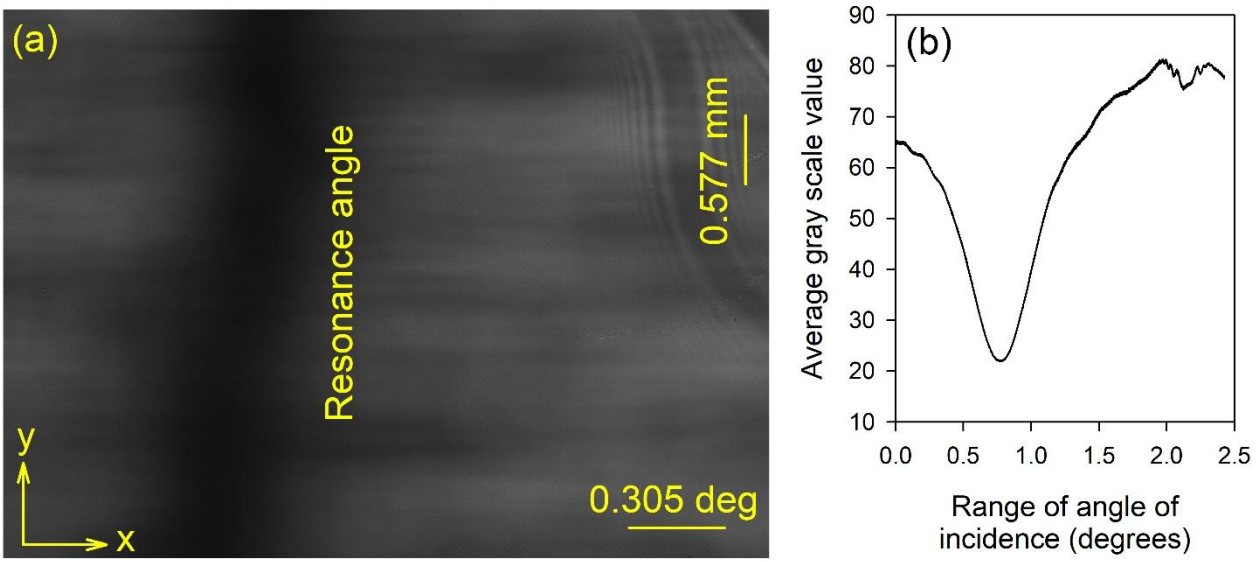

Figure 5: Typical (a) 2D and (b) 1D output of the LW (TE-polarised light was used, the average gray scale value is indicative of the reflectivity of the LW, and was calculated by taking an average of the gray scale values along the width of the microchannel at each angle of incidence)

Refractive Index Sensitivity (RIS), reproducibility and RI resolution: RIS is the slope of the calibration curve of shift in resonance angle ($\Delta\theta_R$) *versus* RI, and has the unit of ° RIU^{-1}. RI resolution provides the minimum change in RI that can be measured using a combination of a sensor and read-out instrumentation. For a selected sensor, the RI resolution to some extent can be improved by reducing the size of each pixel on a camera used to capture the sensor output and/or increasing the distance of the camera from the sensor. Alternatively, a zoom lens could be interposed between the sensor and camera, although this would be a significantly more expensive option. The RI resolution can be used to estimate the limit of detection (LOD) of a protein of molecular weight, M_w, and known refractive index increment (i.e. dn/dc which is the rate of change of refractive index of the protein with respect to its concentration). More specifically, LOD = (RI resolution)×$(dn/dc)^{-1}$×$(M_w)^{-1}$. The figure of merit (FOM) is the RIS divided by the full width at half maximum (FWHM) of the reflectivity dip, and has the units RIU^{-1}.

A typical sensorgram showing $\Delta\theta_R$ *versus* time as different concentrations of glycerol solutions were introduced on the waveguide is shown in Figure 6. It took 300±5 s for each glycerol solution to reach the LW device from the time point at which a change in concentration of glycerol solution occurred. This time delay was determined by the distance between the two ends of the tubing; one of which was immersed in the solution and the other was connected to the inlet of the flowcell mounted on the LW. The other factor that determined the time delay was the flow rate of the solution that was set using the peristaltic pump. Each step in Figure 6 was observed 300±5 s after the time at which a change in concentration of glycerol solution occurred and hence provided the shift in the resonance angle of the LW corresponding to each concentration of glycerol solution.

The different traces represent the response of the LW to glycerol solutions across the width of the microchannel. As different traces in Figure 6 followed each other quite closely, the response of the LW to glycerol solutions across the width of the microchannel was uniform. Additionally, as shown in the inset in Figure 6, linear relationship was observed between $\Delta\theta_R$ and RI of glycerol solutions. The relationship for one of the LWs tested is given by $\Delta\theta_R = -159.22 + 119.19\times RI°$ with "r" of 0.9998 where "r" is Pearson correlation coefficient. This implies that the RIS of the LW determined using the 3D printed instrument is 119.19 ° RIU^{-1}, which is comparable to the value previously obtained using the laboratory-based instrumentation for LWs [8, 16, 19]. The FWHM of the dip is ~0.8°, which gives a FOM of ~149 RIU^{-1}. This is significantly better than SPR comprising a low refractive index porous silica film deposited on metal to improve the FOM (~149 RIU^{-1} *versus* ~45 RIU^{-1}) [39].

As shown in Table 2, the area-to-area and chip-to-chip variability of the RIS of the LW was <10%. The RIS values along with an average of three times the noise on $\Delta\theta_R$ at equilibrium for all glycerol solutions obtained using the 3D printed and laboratory based instruments was subsequently used to determine the RI resolution of the two instruments. The RI resolution of the 3D printed and existing laboratory based instrumentations fabricated by CNC machining was 2.37×10^{-6} and 5.90×10^{-6} RIU respectively. Thus, the RI resolution of the two instruments was broadly comparable. The RI resolution of the LW obtained using the 3D printed instrument was comparable to the values reported in literature for 3D printed SPR instrument [30-36] (2.37×10^{-6} RIU *versus* 1.7×10^{-6} RIU). Based on the RI resolution of the LW obtained using the 3D printed instrument and typical (dn/dc) of 1.89×10^{-4} L g^{-1} for proteins [40], we estimate the LOD for IgG (M_w: 150,000 g) to be ~83 nM in the absence of antibodies to enhance the local concentration of protein in the waveguide.

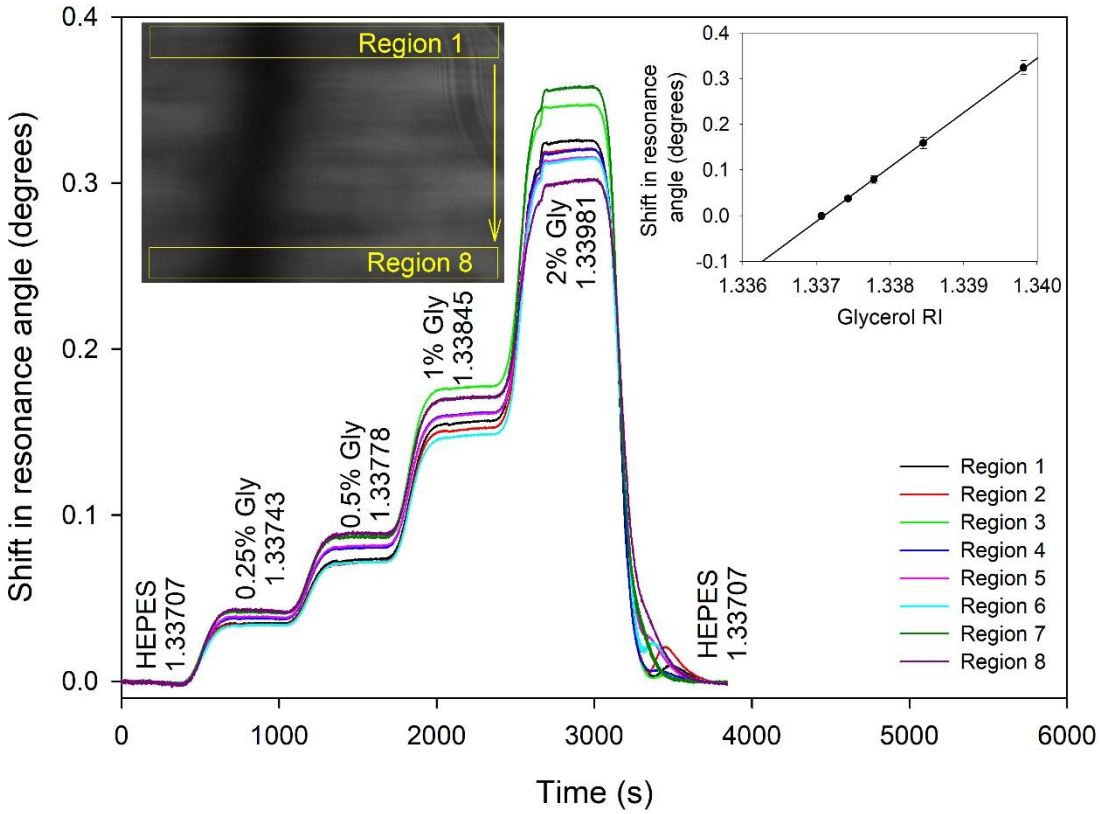

Figure 6: Sensorgram for glycerol solutions of different concentrations (insets show a plot of $\Delta\theta_R$ *versus* RI of glycerol solutions and error bars represent variations in response of the LW to glycerol solutions along the width of the microchannel, and the location of 8 regions corresponding to different colour traces on the LW output)

Description	RIS (° RIU^{-1})
LW 1	119 ± 6
LW 2	121 ± 7
LW 3	120 ± 5
Average of LW 1, LW 2 and LW 3	120 ± 11

Table 2: A summary of the RIS where area-to-area and chip-to-chip variability was calculated using 10 regions/ LW and 3 LWs respectively (where LW 1, LW 2 and LW 3 are three different LW devices)

Sensing of protein-based analytes:

A 1% chitosan film LW was divided into 8 equal regions along the width of the microchannel and the change in resonance angle ($\Delta\theta_R$) was monitored as various protein solutions were added, ultimately leading to the detection of IgG. The chitosan waveguide was flushed with an excess of

GA, which is a very reactive cross-linker. Thus, the free amines in chitosan were readily converted to aldehyde groups, as verified by a shift of 0.41±0.01° (n=8 regions on a LW) in the resonance angle (Figure 7). GA tends to self-polymerise resulting in a continuous drift in the resonance angle and the reaction was terminated by a HEPES buffer wash after 36 min. A shift of 1.54±0.03° (n=8 regions on a LW) in $\Delta\theta_R$ was observed after 2.5 h reaction between 10 mg/ml streptavidin and GA activated waveguide followed by a HEPES buffer wash. The change in the resonance angle because of buffer washes after streptavidin immobilisation was minimal suggesting that the protein was covalently bound to the waveguide. Figure 7 also shows that the change in $\Delta\theta_R$ as a result of 5 mg/ml BSA following streptavidin immobilisation and buffer wash was minimal suggesting that a majority of free aldehydes were used up during streptavidin immobilisation. 0.012 mg/ml (or 77.9 nM) biotin anti-IgG was then immobilized using biotin streptavidin interactions. Finally, 0.02 mg/ml (or 133.3 nM) IgG resulted in a shift of 0.0.04±0.01° (n=8 regions on a LW) in $\Delta\theta_R$ after a buffer wash, implying the protein was bound to anti-IgG.

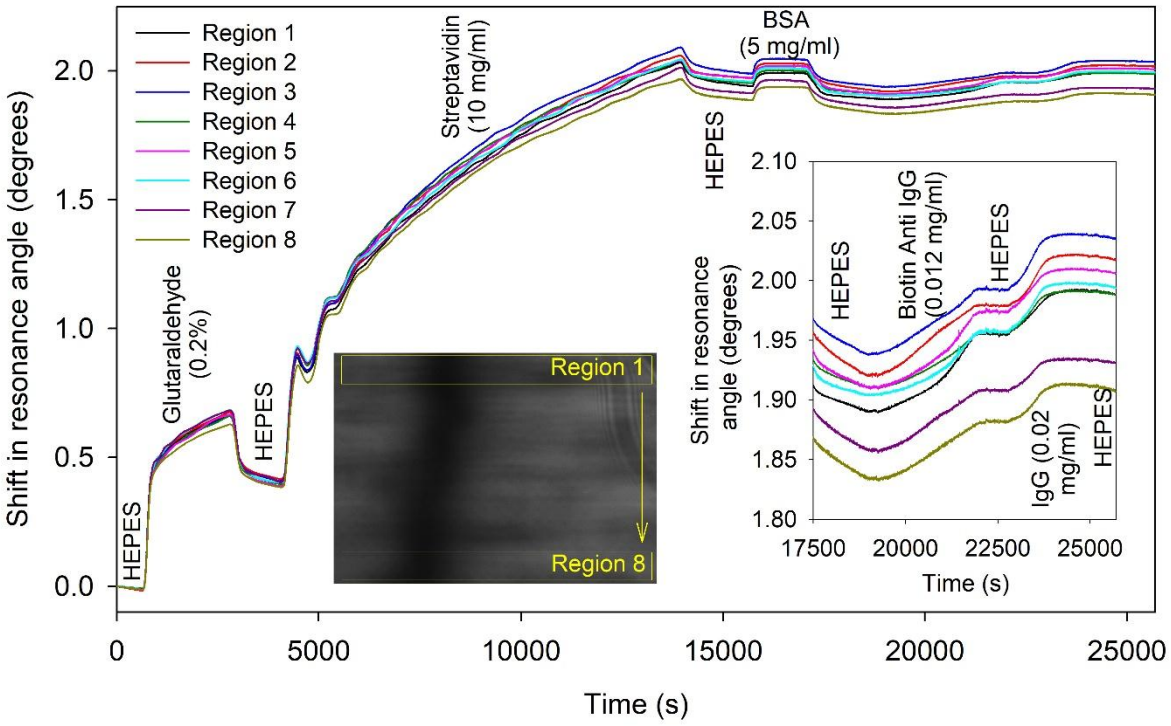

Figure 7: Sensorgram for a protein run (insets show a zoomed view of the selected time interval and the location of 8 regions corresponding to different colour traces on the LW output)

IV. Conclusions

LWs offer significant benefits – improved rejection of common-mode effects for measurement of analytes in complex samples, ease of integration with electric field driven sample processing for

speed and sensitivity, broad wavelength range of operation for information rich data. Additionally, LWs offer comparable sensitivity to SPR, but are fabricated using solution-processing methods and affordable materials. This work has described the successful design and fabrication of a compact and portable 3D printed instrument for LWs to facilitate their application at point-of-use biosensing, and demonstrated its use by sensing protein binding in a chitosan waveguide layer. While this instrumentation is still in development, the results reported in this work suggested comparable sensitivity, lower costs, and significantly improved portability compared to current laboratory-based waveguide instrumentation. This work provides substantial evidence for the successful 3D printing of portable and affordable waveguide instrumentation, which could be manufactured on a larger scale. LW biosensors with 3D printed instrumentation, therefore, are well suited for point-of-use, which in turn has a potential to revolutionise human health, environmental monitoring and food security.

Acknowledgements

The authors acknowledge the funding support from the Engineering and Physical Sciences Research Council (EPSRC) (Grant EP/N02074X/2), EPSRC global challenge research fund (GCRF) and University of Birmingham.

References:

[1] E. B. Bahadir, and M. K. Sezginturk, “Applications of commercial biosensors in clinical, food, environmental, and biothreat/biowarfare analyses,” *Analytical Biochemistry,* vol. 478, pp. 107-120, 2015.

[2] A. Roda, E. Michelini, M. Zangheri *et al.*, “Smartphone-based biosensors: A critical review and perspectives,” *TRAC-Trends in Analytical Chemistry,* vol. 79, pp. 317-325, 2016.

[3] E. Primiceri, M. S. Chiriaco, F. M. Notarangelo *et al.*, “Key enabling technologies for point-of-care diagnostics,” *Sensors,* vol. 18, pp. 3607-1-3607-34, 2018.

[4] D. M. Zhang, and Q. J. Liu, “Biosensors and bioelectronics on smartphone for portable biochemical detection,” *Biosensors & Bioelectronics,* vol. 75, pp. 273-284, 2016.

[5] R. Gupta, and N. J. Goddard, “A polymeric waveguide resonant mirror (RM) device for detection in microfluidic flow cells,” *Analyst,* vol. 138, pp. 3209-3215, 2013.

[6] R. Gupta, and N. J. Goddard, “A proof-of-principle study for performing enzyme bioassays using substrates immobilized in a leaky optical waveguide,” *Sensors and Actuators B-Chemical,* vol. 244, pp. 549-558, 2017.

[7] R. Gupta, and N. J. Goddard, "A novel optical biosensor with internal referencing." pp. 1490-1492, 2013.

[8] R. Gupta, N. Alamrani, G. M. Greenway *et al.*, "A method for determining average iron content of ferritin by measuring its optical dispersion," *Analytical Chemistry,* vol. 91, pp. 7366-7372, 2019.

[9] J. Homola, "Surface plasmon resonance sensors for detection of chemical and biological species," *Chemical Reviews,* vol. 108, pp. 462-493, 2008.

[10] A. Dutta, "Brief review on integrated planar waveguide-based optical sensor," *Planar Waveguide Optical Sensors: From Theory to Applications*, Engineering Materials, pp. 9-69, Berlin: Springer-Verlag Berlin, 2016.

[11] R. A. Potyrailo, S. E. Hobbs, and G. M. Hieftje, "Optical waveguide sensors in analytical chemistry: today's instrumentation, applications and trends for future development," *Fresenius Journal of Analytical Chemistry,* vol. 362, pp. 349-373, 1998.

[12] K. Schmitt, K. Oehse, G. Sulz *et al.*, "Evanescent field sensors based on tantalum pentoxide waveguides - a review," *Sensors,* vol. 8, pp. 711-738, 2008.

[13] C. A. Barrios, "Optical slot-waveguide based biochemical sensors," *Sensors,* vol. 9, pp. 4751-4765, 2009.

[14] H. Mukundan, A. S. Anderson, W. K. Grace *et al.*, "Waveguide-based biosensors for pathogen detection," *Sensors,* vol. 9, pp. 5783-5809, 2009.

[15] R. Ulrich, and W. Prettl, "Planar leaky light-guides and couplers," *Applied Physics,* vol. 1, pp. 55-68, 1973.

[16] R. Gupta, and N. J. Goddard, "Broadband absorption spectroscopy for rapid pH measurement in small volumes using an integrated porous waveguide," *Analyst,* vol. 142, pp. 169-176, 2017.

[17] R. Gupta, B. Bastani, N. J. Goddard *et al.*, "Absorption spectroscopy in microfluidic flow cells using a metal clad leaky waveguide device with a porous gel waveguide layer," *Analyst,* vol. 138, pp. 307-314, 2013.

[18] R. Gupta, and N. J. Goddard, "A novel leaky waveguide grating (LWG) device for evanescent wave broadband absorption spectroscopy in microfluidic flow cells," *Analyst,* vol. 138, pp. 1803-1811, 2013.

[19] R. Gupta, and N. J. Goddard, "Optical waveguide for common path simultaneous refractive index and broadband absorption measurements in small volumes," *Sensors and Actuators B-Chemical,* vol. 237, pp. 1066-1075, 2016.

[20] N. J. Goddard, and R. Gupta, "Speed and sensitivity – integration of electrokinetic preconcentration with a leaky waveguide biosensor," *Sensors and Actuators B - Chemical,* vol. 301, pp. 127063, 2019.

[21] D. B. Kell, and E. Pretorius, "Serum ferritin is an important inflammatory disease marker, as it is mainly a leakage product from damaged cells," *Metallomics,* vol. 6, pp. 748-773, 2014.

[22] N. A. Alamrani, G. M. Greenway, N. Pamme *et al.*, "A feasibility study of a leaky waveguide aptasensor for thrombin," *Analyst,* vol. 144, pp. 6048-6054, 2019.

[23] C. Culmone, G. Smit, and P. Breedveld, "Additive manufacturing of medical instruments: A state-of-the-art review," *Additive Manufacturing,* vol. 27, pp. 461-473, 2019.

[24] T. D. Ngo, A. Kashani, G. Imbalzano *et al.*, "Additive manufacturing (3D printing): A review of materials, methods, applications and challenges," *Composites Part B-Engineering,* vol. 143, pp. 172-196, 2018.

[25] J. Y. Lee, J. An, and C. K. Chua, "Fundamentals and applications of 3D printing for novel materials," *Applied Materials Today,* vol. 7, pp. 120-133, 2017.

[26] Z. X. Khoo, J. E. M. Teoh, Y. Liu *et al.*, "3D printing of smart materials: A review on recent progresses in 4D printing," *Virtual and Physical Prototyping,* vol. 10, pp. 103-122, 2015.

[27] Y. Y. Xu, X. Y. Wu, X. Guo *et al.*, "The boom in 3D-printed sensor technology," *Sensors,* vol. 17, pp. 1166-1-1166-7, 2017.

[28] A. Lambert, S. Valiulis, and Q. Cheng, "Advances in optical sensing and bioanalysis enabled by 3D printing," *ACS Sensors,* vol. 3, pp. 2475-2491, 2018.

[29] T. Han, S. Kundu, A. Nag *et al.*, "3D printed sensors for biomedical applications: a review," *Sensors,* vol. 19, pp. 1706-1-1706-22, 2019.

[30] M. Somarapalli, R. Jolivot, and W. Mohammed, "Realization of low-cost multichannel surface plasmon resonance based optical transducer," *Photonic Sensors,* vol. 8, pp. 289-302, 2018.

[31] C. G. Zhang, C. J. Chen, K. Settu *et al.*, "Angle-scanning surface plasmon resonance system with 3D printed components for biorecognition investigation," *Advances in Condensed Matter Physics,* vol. 2018, pp. 1-7, 2018.

[32] C. A. de Souza, A. M. N. Lima, and H. Neff, *Smartphone based, portable optical biosensor utilizing surface plasmon resonance*, pp. 890-895, 2014.

[33] S. Rampazzi, G. Danese, F. Leporati *et al.*, "A localized surface plasmon resonance-based portable instrument for quick on-site biomolecular detection," *IEEE Transactions on Instrumentation and Measurement,* vol. 65, pp. 317-327, 2016.

[34] S. Tonello, G. Abate, M. Borghetti *et al.*, "Wireless point-of-care platform with screen-printed sensors for biomarkers detection," *IEEE Transactions on Instrumentation and Measurement,* vol. 66, pp. 2448-2455, 2017.

[35] I. Hussain, and P. Nath, “Design of a 3D printed compact interferometric system and required phone application for small angular measurements,” *Review of Scientific Instruments,* vol. 89, pp. 103111-1-103111-8, 2018.

[36] V. N. Konopsky, and E. V. Alieva, “Imaging biosensor based on planar optical waveguide,” *Optics and Laser Technology,* vol. 115, pp. 171-175, 2019.

[37] R. Signini, and S. P. Campana, “On the preparation and characterization of chitosan hydrochloride,” *Polymer Bulletin,* vol. 42, pp. 159-166, 1999.

[38] W. Hoffman, F. G. Lakkis, and G. Chalasani, “B Cells, antibodies, and more,” *Clinical Journal of the American Society of Nephrology,* vol. 11, pp. 137-154, 2016.

[39] Q.-Q. Meng, X. Zhao, C.-Y. Lin *et al.*, “Figure of merit enhancement of a surface plasmon resonance sensor using a low-refractive-index porous silica film,” *Sensors,* vol. 17, pp. 1846-1-1846-11, 2017.

[40] H. Zhao, P. H. Brown, and P. Schuck, “On the distribution of protein refractive index increments,” *Biophysical Journal,* vol. 100, pp. 2309-2317, 2011.